Pharm Res (2012) 29:1866–1881
DOI 10.1007/s11095-012-0713-9

RESEARCH PAPER

Analysis of a Nanocrystalline Polymer Dispersion of Ebselen Using Solid-State NMR, Raman Microscopy, and Powder X-ray Diffraction

Frederick G. Vogt • Glenn R. Williams

Received: 7 January 2012 / Accepted: 15 February 2012 / Published online: 25 February 2012

ABSTRACT

Purpose Nanocrystalline drug-polymer dispersions are of significant interest in pharmaceutical delivery. The purpose of this work is to demonstrate the applicability of methods based on two-dimensional (2D) and multinuclear solid-state NMR (SSNMR) to a novel nanocrystalline pharmaceutical dispersion of ebselen with polyvinylpyrrolidone-vinyl acetate (PVP-VA), after initial characterization with other techniques.

Methods A nanocrystalline dispersion of ebselen with PVP-VA was prepared and characterized by powder X-ray diffraction (PXRD), confocal Raman microscopy and mapping, and differential scanning calorimetry (DSC), and then subjected to detailed 1D and 2D SSNMR analysis involving ^{1}H, ^{13}C, and ^{77}Se isotopes and ^{1}H spin diffusion.

Results PXRD was used to show that dispersion contains nanocrystalline ebselen in the 35–60 nm size range. Confocal Raman microscopy and spectral mapping were able to detect regions where short-range interactions may occur between ebselen and PVP-VA. Spin diffusion effects were analyzed using 2D SSNMR experiments and are able to directly detect interactions between ebselen and the surrounding PVP-VA.

Conclusions The methods used here, particularly the 2D SSNMR methods based on spin diffusion, provided detailed structural information about a nanocrystalline polymer dispersion of ebselen, and should be useful in other studies of these types of materials.

KEY WORDS confocal Raman microscopy · dipolar spin diffusion · nanocrystalline polymer dispersion · powder X-ray diffraction · solid-state NMR

F. G. Vogt (✉) • G. R. Williams
Product Development, GlaxoSmithKline plc.
709 Swedeland Road
King of Prussia, Pennsylvania 19406, USA
e-mail: fred.g.vogt@gsk.com

INTRODUCTION

The development of amorphous polymer dispersions of active pharmaceutical ingredients (APIs) is a popular approach to improving the dissolution of poorly-soluble compounds by promotion of supersaturated conditions (1,2). Although less commonly encountered, polymer dispersions of crystalline API can also be beneficial in drug development for similar reasons (3–7). Polymers can also be used to modify the physical properties of crystalline APIs to promote wettability, increase powder flow performance, or enhance other bulk powder properties. Beyond the preparation of modified API, polymers can also be used to modify crystallization conditions and affect the final habit obtained (6). The use of crystalline dispersions can potentially address chemical and physical stability issues that can occur with amorphous dispersions while still offering improved dissolution performance. For example, the preparation of rapid-release nanocrystalline indomethacin embedded in microparticles of mannitol coated with L-leucine was recently reported (7). Because of the increasing interest in crystalline solid dispersions, there is motivation to develop analytical methods to study these materials.

Recently, spectroscopic techniques using two-dimensional (2D) solid-state nuclear magnetic resonance (SSNMR) were shown to readily discriminate between the formation of an amorphous molecular dispersion and the presence of a phase-separated mixture (8,9). These techniques, which are based on two NMR phenomena, short-range dipolar coupling and longer-range spin diffusion, offer an alternative method to analysis of molecular mixing in cases where existing approaches are not amendable. This occurs when, for example, the glass transition temperature (T_g) determined by differential scanning calorimetry (DSC) may not be a reliable indicator of dispersion miscibility and stability (10). The SSNMR approaches used for amorphous dispersions can be

extended to the case of crystalline dispersions. However, the presence of crystallinity necessarily requires domains with dimensions on the order of nanometers or greater. Because of this, modified SSNMR methods that are adapted to detection of longer-range spin diffusion interactions may be used to probe spin diffusion in systems with domain sizes on the order of nanometers. Although SSNMR spin diffusion methods are well known and have been applied in many other fields, particularly in studies of heterogeneous polymeric systems, their use in pharmaceutical applications has been limited and to date has primarily focused on short-range structural studies of single-component systems (11–21).

In the present work, 2D SSNMR correlation experiments based on longer-range spin diffusion processes between ^{1}H nuclei are introduced and are shown to be highly useful for detection of interactions between a nanocrystalline API and an amorphous polymer. A dispersion consisting of 50% *w/w* ebselen in polyvinylpyrrolidone-vinyl acetate (PVP-VA) copolymer was chosen to illustrate the approach. Ebselen is an antioxidant and anti-inflammatory API with poor water solubility that has been investigated for the treatment of cerebral infarctions and other conditions (22,23). The structure of ebselen, also known as 2-phenyl-1, 2-benzisoselenazol-3(2H)-one), is shown in Fig. 1a with the atomic numbering scheme used in this work. The chemical structure of the PVP-VA copolymer is shown in Fig. 1b. The dispersion of ebselen in PVP-VA is first determined to be nanocrystalline by powder X-ray diffraction (PXRD) analysis. DSC is found to be of limited use in the characterization of this material because of the tendency of ebselen to dissolve in the PVP-VA at higher temperatures. Confocal Raman microscopic mapping, which is a useful analytical technique for the study of API-polymer dispersions (24), is applied to spatially map the dispersions and demonstrate that the material is primarily crystalline, and also to detect subtle interactions between the API and polymer. ^{13}C and ^{77}Se SSNMR experiments are used to confirm the crystalline nature of the material and investigate NMR properties in more detail including a comparison with a theoretical calculation. 2D SSNMR experiments based on spin diffusion and correlation between ^{1}H and ^{13}C nuclei are then used to show long-range interactions between ebselen and PVP-VA. These experiments potentially have wide applicability to the study of pharmaceutical nanocrystalline dispersions.

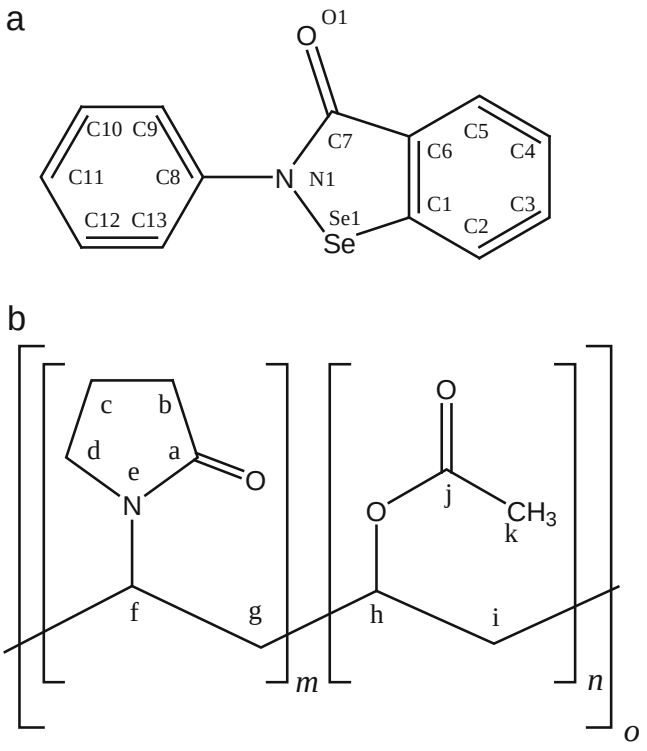

Fig. 1 (**a**) Chemical structure and atomic numbering scheme of ebselen. (**b**) Chemical structure and atomic numbering scheme of PVP-VA.

MATERIALS AND METHODS

Preparation of Materials

A 50% *w/w* dispersion of ebeselen in PVP-VA was prepared by physically mixing 43.0 mg of ebselen (Sigma-Aldrich Co., St. Louis, MO, USA) with 44.0 mg of PVP-VA64 (BASF GmbH, Ludwigshafen, Germany). The solids were dissolved in 3 mL of acetone with gentle shaking and mild heating. A yellow solution was obtained, which was kept in solution for 20 min prior to rapid vacuum drying on a 10 cm watch glass. The solution was evaporated within 1 min, and the solids were subsequently dried for 24 h at 50°C. The dried solids were scraped and recovered for analysis.

PXRD Analysis

PXRD patterns were obtained using an X'Pert Pro diffractometer using Debye-Scherrer transmission geometry with a focusing mirror and an X'Celerator real time multi-strip detector (PANalytical B.V., Almelo, The Netherlands) with a maximum active length of 2.122°. Samples were loaded into 0.91 mm (inner diameter) polyimide capillaries and analyzed at ambient temperature and humidity. CuKα radiation (1.542 Å) was used with a generator power and current of 45 kV and 40 mA, respectively. Samples were scanned in continuous mode from 3 to 40°θ with a 2θ step size of 0.0167°. The sample was rotated in a capillary spinner at a rate of >1000 rpm. The incident beam path was equipped with a focusing mirror, 0.02 radian Soller slit, and a 0.5° fixed divergence slit. The diffracted beam path was equipped with a programmable anti-scatter slit (fixed at 0.25°), and a 0.02 radian Soller slit.

Pawley refinement (25) of the PXRD data was performed using the Reflex module within the Materials Studio version

5.0 software package (Accelrys, San Diego, CA, USA). The unit cell from the previously reported crystal structure of ebselen was used as input for the Pawley refinement (26). X'Pert Highscore Plus version 2.1 (PANalytical B.V., Almelo, The Netherlands) were used to perform Le Bail fitting (27) and peak width analyses.

DSC Analysis

DSC experiments were performed using a Q2000 instrument (TA Instruments, Inc., New Castle, DE, USA). Samples with masses of 3 to 5 mg were heated in closed aluminum pans with lids that were not crimped. Nitrogen was used as purge gas with a flow rate of 20 mL/min. Two heating rates of 10°C/min and 0.5°C/min were employed over a temperature range of 25 to 250°C.

Confocal Raman Microscopy

Raman microscopy and mapping was performed using an Aramis confocal Raman spectrometer and microscope system (Horiba Jobin Yvon, Inc., Edison, NJ, USA). The system utilized an Olympus BX41 confocal optical microscope (Olympus America, Inc., Chester Valley, PA, USA). An Olympus U-LH 100 W Hg lamp and U-RFL-T power source were used for brightfield illumination. Optical images were captured using an Infinity 3 cooled charge-coupled device camera (Lumenera Corp., Ottawa, Ontario, Canada). Raman spectra were obtained using a 633 nm HeNe laser. Raman spectral maps were obtained using a ×50 objective with the stage translated in 2 μm steps. A 25×25 map used for this analysis was acquired using 32 accumulations each with 2 s of detector exposure time for a total map acquisition time of 12 h. A confocal hole of 500 μm and a slit width of 100 μm were used. Raman bands used for mapping plots were subjected to baseline correction.

NMR Analysis

SSNMR experiments were performed using two NMR instruments, an Avance spectrometer with a static field of 9.4 T and an Avance III spectrometer with a static field of 16.4 T, operating at ^{1}H frequencies of 399.87 and 700.13 MHz, respectively (Bruker Biospin, Inc., Billerica, MA, USA). ^{13}C and ^{77}Se SSNMR spectra were obtained at 9.4 T using a Bruker 4 mm magic-angle spinning (MAS) probe doubly-tuned to ^{1}H and an X-nucleus frequency of 100.56 MHz for ^{13}C experiments or 76.36 MHz for ^{77}Se experiments. With this probe, experiments were performed using 4 mm zirconia rotors with a nominal volume of 50 μL wherein the sample is restricted to the center of the rotor, which allows for smaller sample sizes of 50 mg and also maximizes RF homogeneity across the sample. Cross-polarization (CP) transfers were performed at radiofrequency power levels of 40 to 80 kHz. The power level was ramped linearly during the contact time on the ^{1}H channel to enhance CP efficiency (28). ^{13}C CP spectra were obtained at an MAS rate (ν_r) of 8 kHz with a five-pulse total sideband suppression (CP-TOSS) sequence (29). ^{77}Se CP-MAS spectra were obtained at ν_r settings of 10 and 14 kHz without sideband suppression. ^{1}H heteronuclear decoupling was performed at an RF power of 105 kHz using the SPINAL-64 pulse sequence (30). Edited ^{13}C spectra containing only quaternary and methyl signals were obtained using dipolar dephasing (also known as non-quaternary suppression or NQS) during the TOSS period and three subsequent rotor periods using a shifted echo pulse sequence (29,31). ^{13}C spectra were referenced to tetramethylsilane (TMS) using an external reference sample of hexamethylbenzene using the methyl peak at 17.36 ppm (32). ^{1}H spectra were referenced by addition of a small amount of liquid TMS to the rotor. ^{77}Se spectra were referenced to an external sample of cadmium selenide (Sigma-Aldrich Co., St. Louis, MO, USA), using the reported chemical shift of −492 ppm for this material (33). The principal components of the CST were obtained via fitting of the ^{77}Se CP-MAS spectrum using the Topspin version 3.0 software package (Bruker Biospin, Inc., Billerica, MA, USA). The reported principal component values follow the convention $\delta_{11} \geq \delta_{22} \geq \delta_{33}$. Proton spin–lattice relaxation times (^{1}H T_1) were determined via ^{1}H saturation recovery with a 100-pulse saturation comb. With ν_r=8 kHz, the ^{1}H T_1 of input crystalline ebselen and the 50% *w*/*w* dispersion of ebselen in PVP-VA were determined to be approximately 12 s and 3 s, respectively. Additional ^{1}H T_1 values were measured at higher ν_r settings and at different static field strengths as discussed below. All experiments were performed with relaxation delays set to three times the ^{1}H T_1 value, which fell generally in the range of 30 s for crystalline ebselen and 10 s for the 50% *w*/*w* dispersion of ebselen in PVP-VA. ^{1}H spectra were obtained using direct polarization at high MAS rates (referred to here as the DP-MAS experiment) using a single excitation pulse without decoupling during acquisition, and were also obtained using the windowed DUMBO homonuclear decoupling sequence during acquisition (34). 2D CP heteronuclear correlation (CP-HETCOR) experiments between ^{1}H and ^{13}C nuclei were obtained using 4-mm probes with ν_r=12.5 and frequency-switched Lee-Goldburg (FSLG) homonuclear decoupling at 105 kHz (35). The HETCOR experiments were performed so that the entire spectrum was recorded with F_1>0 Hz, where F_1 is the indirectly-detected ^{1}H frequency dimension and F_2 is the directly-detected dimension. This approach avoids quadrature images and artifacts in the ^{1}H spectrum at F_1=0 Hz that can occur with this experiment.

Solution-state NMR experiments were performed with the Avance III spectrometer using a 5 mm BBO broadband probe with the inner coil tuned to ^{77}Se at 133.65 MHz and

the outer coil tuned to ^{1}H at 700.13 MHz (Bruker Biospin, Inc., Billerica, MA, USA). Ebselen was dissolved in $CDCl_3$ at a concentration of approximately 20 mg/mL and analyzed at 298 K. The ^{77}Se pulse width was 8 μs and ^{1}H decoupling was not used. A total of 1024 scans were collected using a relaxation delay of 5 s, requiring 1.5 h of acquisition time.

Density Functional Theory Calculations

Prior to NMR chemical shielding calculations, the DMol^3 density functional theory (DFT) package (36,37) implemented in Materials Studio version 5.0 was used to optimize the hydrogen atom positions in the crystal structure of ebselen (26) via a periodic boundary condition calculation (Accelrys Software, Inc., San Diego, CA, USA). For this purpose, the HCTH/407 generalized gradient approximation (GGA) density functional (also known as the HCTH functional) (38) and a double numerical basis set with polarization functions on all atoms (the DNP basis set) were utilized because of their accuracy in reproducing molecular geometry (39). The heavy atom positions and unit cell dimensions remained fixed during the HCTH/DNP optimization and space group symmetry was enforced. A gas-phase cluster comprising two ebselen molecules was extracted from the optimized periodic structure. The cluster consisted of a molecule used for the ^{77}Se CST values and a second molecule included so that its carbonyl oxygen could interact with the selenium atom of the first molecule, as described below. The Gaussian 09W package (Gaussian, Inc., Wallingford, CT, USA) was used for gauge-including atomic orbital (GIAO) NMR shielding calculations on the two-molecule cluster using the B3LYP hybrid density functional (40–42). A locally-dense 6-311++G(3df) Gaussian basis set was used on the selenium atom from which the reported ^{77}Se chemical shielding results were obtained, while the 6-311++G (2d,p) basis set was used on all other atoms. The 2nd-order Douglass-Kroll-Hess approximation was applied during the calculation to account for relativistic effects, which can affect the chemical shielding of ^{77}Se nuclei (43,44).

RESULTS AND DISCUSSION

PXRD and DSC Analysis

Initial characterization of the 50% *w/w* dispersion of ebselen in PVP-VA was performed using PXRD and DSC. Capillary PXRD patterns of the input crystalline phase of ebselen and the 50% *w/w* dispersion of ebselen in PVP-VA are shown in Fig. 2a and b, respectively. The PXRD pattern of crystalline input ebselen was found to match that predicted from the single crystal structure reported for this compound, as shown in Fig. 2a (26). The fitted diffraction pattern in Fig. 2a was the result of a Pawley refinement (25) and shows no significant features that were not modeled. A weighted-profile residual value (R_{wp}) of 4.62% and a non-weighted residual value (R_p) of 3.51% were obtained from the Pawley fit (45). This initial fit of the crystalline input material included a polynomial background, pseudo-Voigt peak shape profiles, a Debye-Scherrer line shift correction and a Finger-Cox-Jephcoat asymmetry correction. The agreement between the experimental and calculated patterns seen in Fig. 2a demonstrates that the ebselen phase used as input here is the same as that determined by single-crystal X-ray diffraction (SCXRD). This crystalline form, also known by its Cambridge Structural Database (CSD) reference code SENGOH (46), can be produced by crystallization from diethyl ether and acetone (26).

The PXRD pattern of the 50% *w/w* dispersion of ebselen in PVP-VA obtained from acetone evaporation is depicted in Fig. 2b. The pattern shows the presence of numerous reflections that match those in crystalline ebselen superimposed on a broad diffusive scattering pattern caused by amorphous PVP-VA. This indicates that the crystalline form of ebselen previously determined by SCXRD analysis persists in the dispersion. However, these reflections are significantly broadened relative to the crystalline pattern in Fig. 2a. This is also evidenced by comparison of the PXRD pattern of the 50% *w/w* dispersion of ebselen in PVP-VA with that of a physical mixture of 50% *w/w* crystalline ebselen and PVP-VA by gentle mechanical mixing of small amounts of the two materials, as shown in Fig. 2b. The broadening observed in the pattern of the dispersion provides an initial indication of nanocrystalline-sized ebselen domains, as significant PXRD broadening is known to occur in this size range (47).

The broadening of reflections in the PXRD pattern of the dispersion in Fig. 2b can be used to estimate the domain size of the crystalline phase (47). Crystallite size broadening can be quantitatively analyzed using the Scherrer equation (47):

$$\Delta(2\theta) = \frac{\lambda}{L_c \cos\theta}$$

where $\Delta(2\theta)$ is the broadening of the diffraction pattern caused by crystallite size (assumed to be Lorentzian), λ is the X-ray wavelength (1.542 Å), and L_c is the average size of the crystallites (which are assumed to be cubic). To calculate the effects of broadening using this equation, the previously-discussed Pawley fit of the input crystalline sample shown in Fig. 2a was used as a starting point. The parameters from the initial Pawley fit capture instrumental broadening effects under the assumption that the input crystalline ebselen has infinite crystallite size. This is a good assumption in the present case because the crystalline input batch showed the presence of large crystals by optical microscopy. Using the parameters from the initial fit, the broadened PXRD pattern in Fig. 2b was then fitted. The only parameters that were allowed to vary

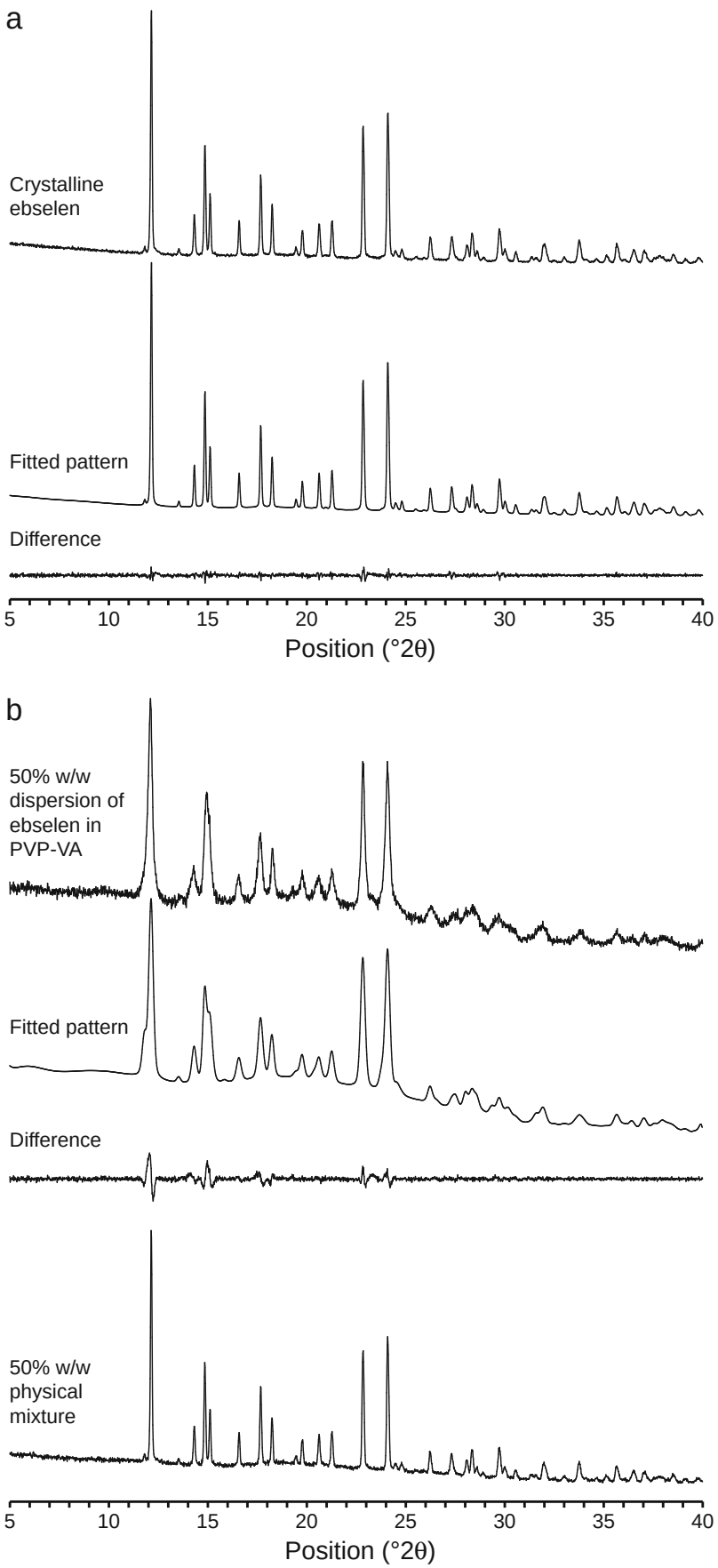

Fig. 2 (**a**) Capillary transmission PXRD pattern of the crystalline ebselen used as input in this study, compared to a calculated pattern from a Pawley fit (R_{wp}=4.62%) of the crystal structure given in Ref. 26 against the experimental pattern. The difference between the fitted and experimental pattern is also shown. (**b**) PXRD patterns of the 50% *w/w* dispersion of ebselen in PVP-VA compared to a Pawley fit with size broadening (R_{wp}=5.94%) and also a 50% *w/w* physical mixture of ebselen and PVP-VA.

were the crystallite size parameters from the Scherrer equation and the polynomial baseline correction to account for diffuse scattering from amorphous PVP-VA. The peak shape parameters, Debye-Scherrer line shift correction, asymmetry, and unit cell dimensions were fixed. Incorporation of the Scherrer equation into the second fit successfully reproduced the broadened pattern, as shown in Fig. 2b, and achieved an R_{wp} of 5.94% and an R_p of 4.18%. The fit yielded an L_c of 37 nm, demonstrating the nanocrystalline nature of the dispersion.

Additional peak broadening analyses of the experimental PXRD pattern of the dispersion were applied to confirm these results. These analyses also utilized the Scherrer equation but obtained $\Delta(2\theta)$ by two different methods, Le Bail fitting (27) and averaged multiple single peak analyses. In both cases the input crystalline material and the broadened samples were analyzed to obtain the full-width half-maximum (FWHM) $\Delta(2\theta)$ (in radians) to capture the broadening of the diffraction pattern caused by decreased crystallite size. Again, the input crystalline material was assumed to have infinite crystallite size and therefore represents the instrumental limitations. The broadening or increase in the linewidth of the dispersion sample peaks compared to the input crystalline peaks was then used to determine $\Delta(2\theta)$ and calculate crystallite size L_c, where λ is the X-ray wavelength (1.542 Å) and θ is the Bragg angle of the analyzed peaks (or the average value of a total θ region as was the case for Le Bail fitting, which afforded an averaged value for FWHM for all peaks). The results for Le Bail fitting yielded an average crystallite size L_c of 49 nm. The results for single peak analyses at 2θ peak positions of 12.2, 17.6, 18.2, and 22.8 yielded an average crystallite size L_c of 61 nm. The consistency of the results from the different methods suggests that the nanocrystalline ebselen in the 50% *w/w* dispersion has a domain size in the range of approximately 35 to 60 nm.

DSC analysis was also performed on the crystalline 50% *w/w* dispersion of ebselen in PVP-VA. DSC has been previously used to estimate domain size in nanocrystalline materials (48,49). Crystalline ebselen was observed to melt with a sharp endotherm with a peak at 181.6°C using a 0.5°C/min heating rate. Analysis of the 50% *w/w* physical mixture of crystalline ebselen in PVP-VA showed indications of dissolution of ebselen in the polymer at higher temperatures. At a heating rate of 10°C/min, the 50% *w/w* physical mixture showed a broad endotherm with a peak at 174°C; this endotherm became barely detectable and shifted to 166°C at a heating rate of 0.5°C/min. The reduction in melting point and in the enthalpy of the endothermic transition in the presence of PVP-VA suggests that the polymer has largely dissolved the crystalline ebselen as temperature increases. This finding renders DSC inapplicable to the size estimation of the nanocrystalline dispersion of interest here (48,49). Although not used to estimate domain size, a broadened endotherm was observed for the 50% *w/w* dispersion with a peak at 165–167°C, depending on the heating rate, confirming the presence of crystallinity. The DSC results also suggest that it may be possible to prepare amorphous nanocrystalline ebselen in PVP-VA by hot-melt extrusion or similar methods, although this possibility was not investigated further.

Confocal Raman Microscopy and Mapping

The crystalline dispersion of ebselen in PVP-VA was examined using confocal Raman microscopy and mapping to assess homogeneity. Although the domain size of the nanocrystalline ebselen is well below the resolution of this technique (which is limited by diffraction effects at optical wavelengths), Raman microscopy can still be used to perform spatially-resolved spectroscopic mapping of the relative concentrations of different chemical components in dispersions (24,50). In Fig. 3, Raman spectra obtained via confocal microscopy of pure PVP-VA and ebselen are compared to two points taken from a 25×25 map of the 50% *w/w* dispersion. Using a 633 nm laser, the Raman scattering intensity of crystalline ebselen, measured in terms of detector counts for the largest peak in each spectrum, was approximately 32 times that of PVP-VA. This is expected from the dominance of aromatic groups and hyperpolarizable bonds in ebselen relative to PVP-VA, and leads to strongly enhanced Raman signals for ebselen in comparison to PVP-VA despite their equal concentrations in the dispersion, as seen in the spectra of Points 1 and 2 in Fig. 3.

In Fig. 4, a Raman spectral map is shown for selected bands detected in the 50% *w/w* dispersion of ebselen in PVP-VA. The map sampled 25×25 points in the x and y directions by moving the stage in 2 μm increments. The color scheme used in Fig. 4 is matched to the bands marked in Fig. 3. The red map depicts band area between 915 and 940 cm^{-1}, which is the strongest band in the Raman spectrum of PVP-VA shown in Fig. 3. The green map shows band area in the region of 1700 to 1760 cm^{-1}, representing the vinyl acetate carbonyl band specific to PVP-VA. The purple map shows band area between 985 and 1005 cm^{-1}, which arises from a band specific to crystalline ebselen as shown in Fig. 3. All of these bands are present in the spectra of both Point 1 and Point 2 in Fig. 3, although the PVP-VA bands are too weak to easily observe in the spectrum of Point 1. Although the particle domain size is well below the spatial resolution of Raman microscopy, comparison of these maps indicates that ebselen and PVP-VA are distributed differently within the "effective" spot size achieved via mapping (50). The Raman bands characteristic of crystalline ebselen were observed in all 625 points in the map, and bands for PVP-VA were observed in nearly all of the points albeit with reduced intensity relative to the strong bands arising from ebselen.

A number of points obtained in the Raman spectral map of the dispersion showed the presence of a Raman band that does not align with either crystalline ebselen or PVP-VA.

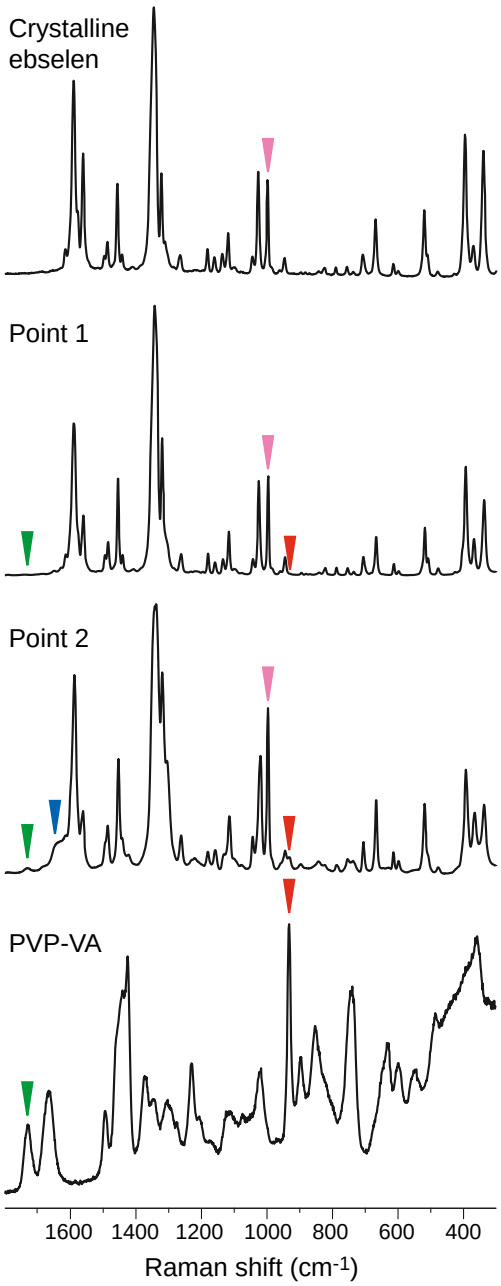

Fig. 3 Raman spectra obtained by confocal microscopic analysis of crystalline ebselen, PVP-VA, and two points in the crystalline dispersion, obtained using a × 50 objective and 633 nm laser excitation. The spectra labeled Point 1 and 2 refer to the map points shown in Fig. 3. Arrowheads denote bands of interest, with colors corresponding to the Raman spectral maps in Fig. 4 (see text).

This broad Raman band is easily seen in the spectrum of Point 2 in Fig. 3 at approximately 1610 cm^{-1} to 1650 cm^{-1} and is denoted by a blue arrow. A spatial map of the area of this band, shown in blue in Fig. 4, suggests that its distribution spatially correlates with that of PVP-VA by comparison with the green and red maps, and not with the crystalline ebselen band distribution shown in the purple map. Given the spatial distribution of this signal, the strong Raman scattering from ebselen, the increased width of the band, and its Raman shift (which is near to that of a strong Raman band from ebselen), this band is tentatively assigned to an amorphous ebselen phase dispersed in the PVP-VA, possibly as a molecular dispersion. Based on the Raman signal intensity, only a small portion of the ebselen is present in this state. The DSC results, which showed evidence of increasing dissolution of ebselen in PVP-VA at higher temperatures, also support this hypothesis assuming that ebselen can dissolve in PVP-VA to some extent at lower temperatures. Although not pursued in the present work, this suggests that the use of a higher temperature process (such as hot melt extrusion) may offer an avenue towards preparation of an amorphous dispersion of ebselen in PVP-VA.

^{13}C and ^{77}Se SSNMR Spectroscopy

With the domain size and homogeneity of the 50% *w/w* dispersion of ebselen in PVP-VA assessed, initial SSNMR studies were performed. ^{13}C CP-TOSS spectra of crystalline ebselen, PVP-VA, and the dispersion are shown in Fig. 5. The ^{13}C spectral assignments given in Fig. 5 refer to the numbering schemes previously shown for ebselen and PVP-VA in Fig. 1. A number of ^{13}C resonances for ebselen and PVP-VA can be assigned as shown in Fig. 5 based on established ^{13}C chemical shift trends (51). Significant spectral overlap in the region between 125 and 131 ppm prevents assignments of specific resonances to the C2, C3, C4, C5, and C11 positions, which are labeled "aromatics" in Fig. 5. The ^{13}C CP-TOSS spectrum of the 50% *w/w* dispersion of ebselen in PVP-VA is consistent with a physical mixture of the two individual components shown in the other spectra. Relative to the individual components, the dispersion shows minor changes in lineshape for the ebselen peaks. Like Raman spectroscopy, SSNMR spectroscopy is sensitive to short range order, so that the nanocrystalline nature of the ebselen does not show major effects on the spectrum. This contrasts with the PXRD results shown in Fig. 2, which are affected by the sensitivity of this technique to long range order. The ^{13}C spectra of crystalline ebselen and the dispersion show broadened resonances most likely from the effects of anisotropic bulk magnetic susceptibility (ABMS) caused by the dominance of aromatic rings in the structure of ebselen and their alignment in the crystal structure (52). The dilution level of ebselen in PVP-VA does not strongly narrow the linewidth of these resonances, most likely because this dilution level is insufficient to limit the effects of ABMS or because it is partly canceled by additional broadening from the nanometer-sized domains and crystal defects. For example, the full width at half maximum of the signal assigned to C7 reduces from 120 Hz in crystalline ebselen to 105 Hz in the dispersion. This is consistent with ABMS dilution effects observed for other aromatic small molecules (53,54).

The ^{13} CP-TOSS spectrum of the 50% *w/w* dispersion of ebselen in PVP-VA shows signal intensity changes relative to

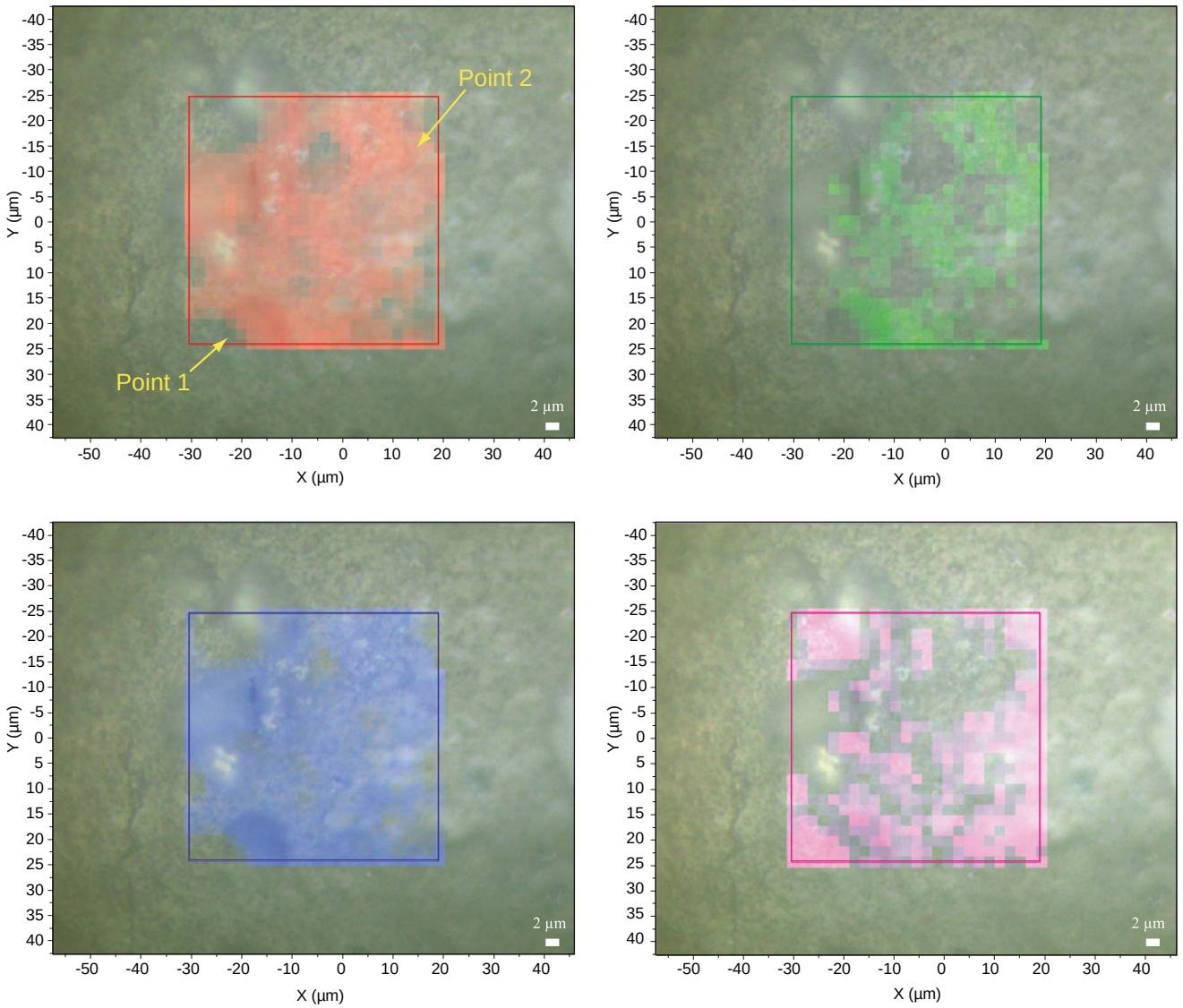

Fig. 4 Raman spectral maps obtained by confocal microscopic analysis of a region of a particle from the dispersion containing 50% *w/w* ebselen. The maps consist of 25 × 25 points analyzed with 2 μm stage increments and were obtained using a × 50 objective and 633 nm laser excitation. The arrows labeled Point 1 and 2 refer to the two map points for which spectra are shown in Fig. 3. The red map shows band area between 940 and 915 cm^{-1} (corresponding to PVP-VA), the green map shows band area between 1700 and 1760 cm^{-1} (PVP-VA), the purple map shows band area between 985 and 1005 cm^{-1} (ebselen) and the blue map shows band area between 1650 and 1610 cm^{-1} (see text). Brighter colors correspond to stronger band intensities.

the similarly-obtained spectrum of crystalline ebselen, most notably the enhanced signal intensity observed for a peak at 130 ppm, denoted by an arrow in Fig. 5. The dipolar dephasing spectrum of the dispersion shown in Fig. 5, which suppresses resonances not arising from quaternary and methyl carbon sites, helps identify this enhanced resonance as C6. This effect is likely caused by interactions between PVP-VA and ebselen at a 2 ms contact time used for this experiment. This effect is more clearly observed in the 2D experiments described in detail in the next section.

The ^{77}Se SSNMR spectra of the ebselen dispersion were also obtained for comparison with the crystalline dispersion. Like ^{13}C, ^{77}Se is a spin ½ nucleus and yields high resolution spectra (33). The ^{77}Se isotope has a natural abundance of 7.63% (33). ^{77}Se SSNMR has not seen significant reported use in the study of drug molecules, despite inclusion of selenium heterocycles in candidate drugs that are of continued interest in drug development (55). ^{77}Se SSNMR has been employed to some extent in the characterization of other biologically-relevant molecules, such as selenium-substituted amino acids (33,56). The solution-state chemical shift of ebselen in $CDCl_3$ solution has been reported to be 960 ppm; this value was verified during the present work (57). The ^{77}Se CP-MAS spectrum of the 50% *w/w* dispersion is shown in Fig. 6a. The observed spectrum consists of a complex sideband manifold characteristic of a material with a strong anistropic

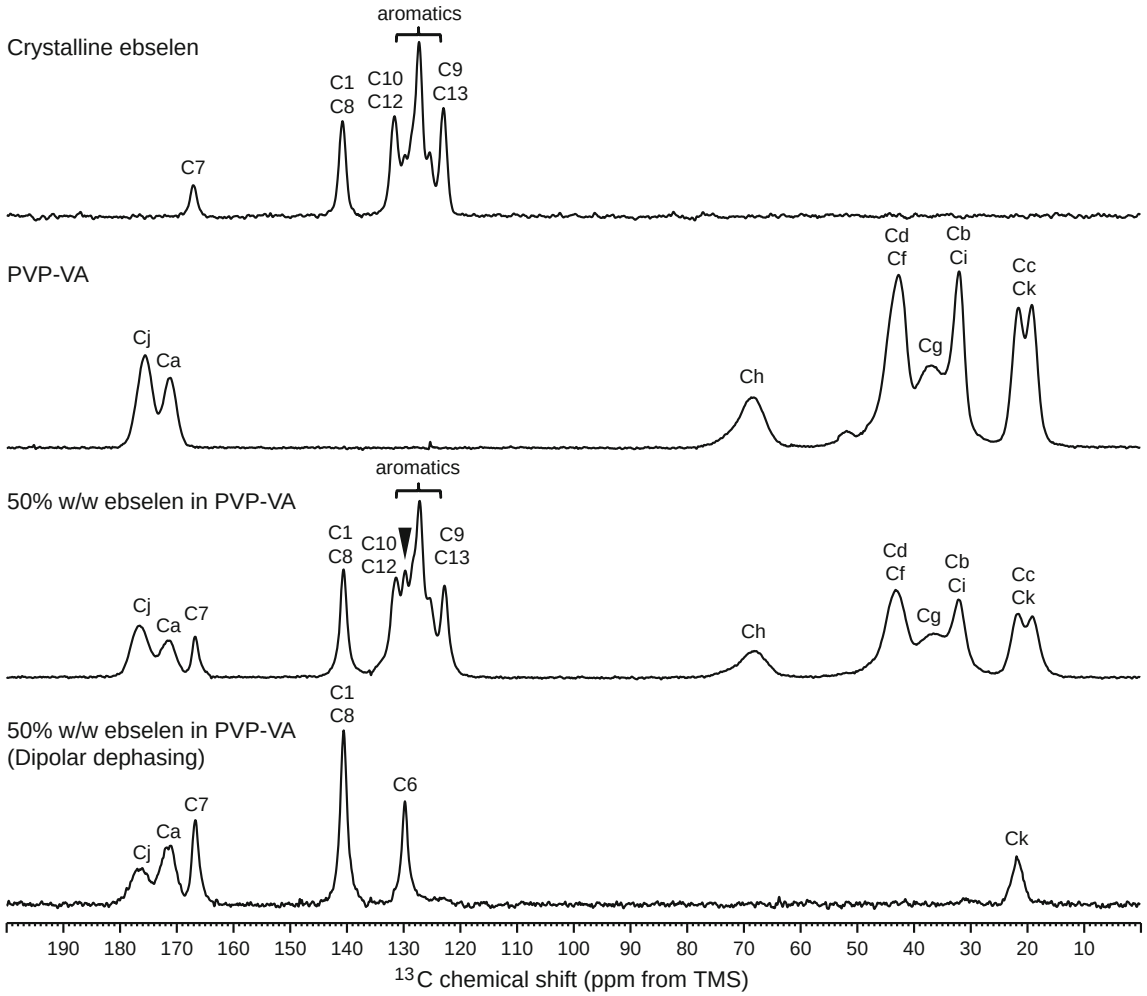

Fig. 5 ^{13}C CP-TOSS spectra (ν_r=8 kHz) of ebselen, PVP-VA, and the 50% *w/w* dispersion of ebselen in PVP-VA. A CP-TOSS spectrum obtained with dipolar dephasing is also shown for the dispersion. The assignments shown refer to the numbering and lettering schemes given for ebselen and PVP-VA in the text. The arrowhead denotes a feature of interest (see text). Spectra were obtained at 9.4 T and 273 K.

chemical shift interaction that dominates even at a high MAS rate and a low static field, as is often the case for selenium (33). ^{77}Se SSNMR spectra for crystalline ebselen have not been previously reported in the literature for comparison. The spinning sideband manifold of crystalline ebselen was indistinguishable from that of the dispersion (not shown). However, in Fig. 6b, the centerbands of crystalline ebselen and the dispersion are compared, and evidence of line broadening can be seen for the dispersion. This broadening is likely the result of defects particularly at the surface of the nanocrystalline ebselen in the dispersion. The isotropic value (δ_{iso}) of the ^{77}Se chemical shift for the dispersion was determined to be 923.8 ppm from dimethylselenide via the peak position of the centerband in Fig. 6b using CdSe as a secondary external reference standard. The spectra in Fig. 6 each required 12 h to obtain.

The ^{77}Se chemical shift tensor (CST) for the dispersion was fitted and analyzed, with the resulting calculated spectrum shown in Fig. 6a. The principal values of the ^{77}Se CST were determined from this fit to be δ_{11}=1696 ppm, δ_{22}=699 ppm, and δ_{33}=377 ppm. From these values, the calculated span (Ω) of the ^{77}Se CST is 1318 ppm and the skew (κ) is −0.51. The selenium site thus exhibits a highly anisotropic chemical shift interaction, which is expected from the limited ^{77}Se SSNMR data reported in the literature for selenoethers and similar systems (33). CST analysis of the ^{77}Se CP-MAS spectrum of crystalline ebselen yielded a similar result (not shown). Because of the lack of literature CST data on compounds similar to ebselen for comparison, a theoretical calculation of ^{77}Se CST parameters was performed. Before the NMR calculation, an optimization of the hydrogen positions from the ebselen crystal structure (26) was performed using a periodic DFT calculation at the HCTH/DNP level of theory, as SCXRD determinations of hydrogen positions are not as accurate as for heavy atoms and even slight errors in geometry can bias calculated CSTs (58,59). A cluster containing two ebselen molecules was extracted from the optimized periodic structure. The cluster consisted of a molecule used for the ^{77}Se

CST values and a second molecule included so that its carbonyl group would interact with the selenium atom on the first molecule. The distance between the oxygen atom (O1) of the carbonyl group and the selenium is 2.571 Å and represents the closest and most significant intermolecular interaction involving the selenium atom (26). The NMR calculation was then performed using the B3LYP hybrid density functional and a locally-dense 6-311++G(3df) basis set on the selenium atom of the first molecule in the cluster, with a 6-311++G(2d,p) basis set used on the remainder of the atoms in the cluster. The ^{77}Se chemical shielding results were referenced to a separate gas-phase calculation of the isotropic ^{77}Se chemical shielding of

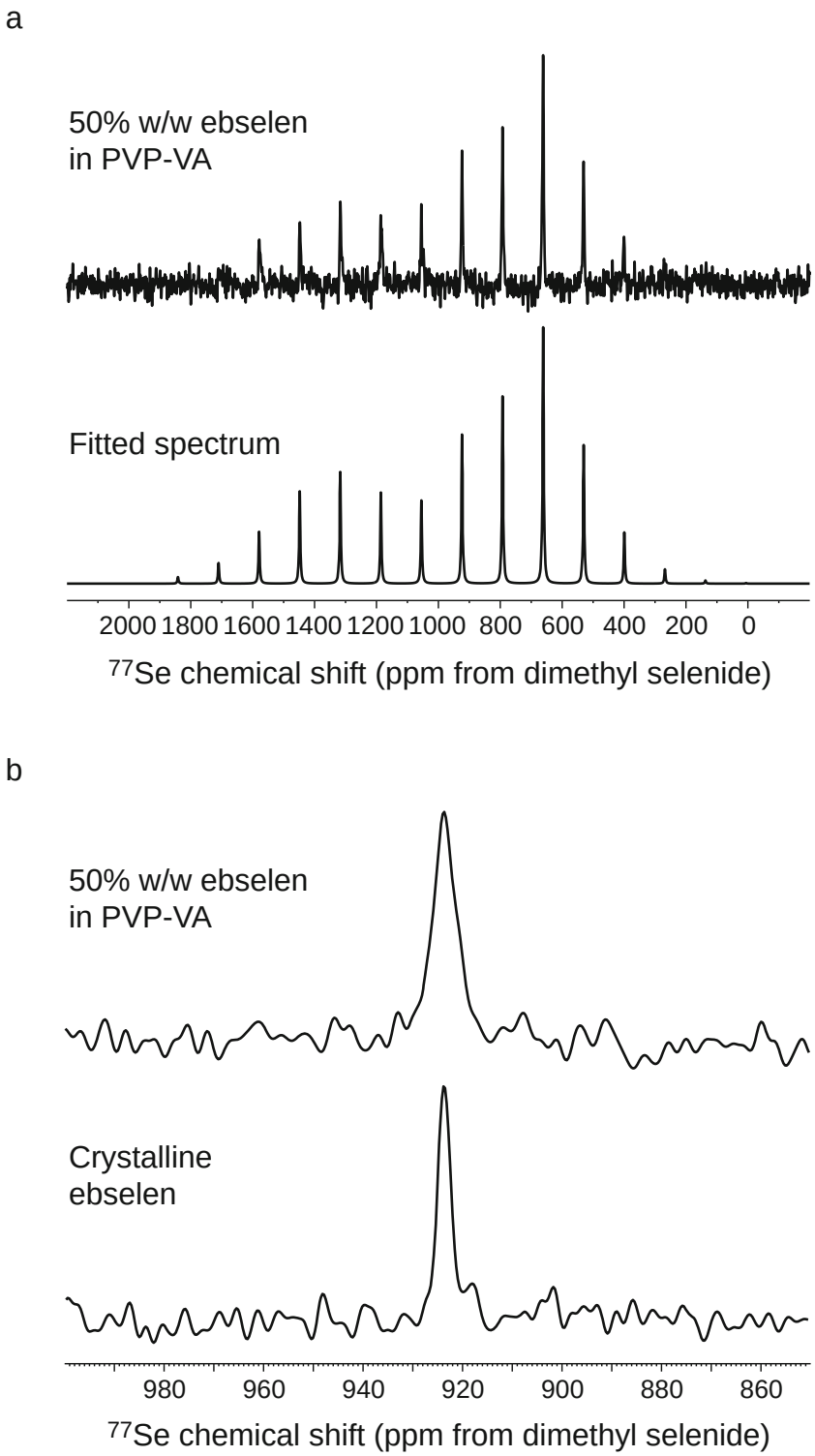

Fig. 6 (**a**) ^{77}Se CP-MAS spectrum (ν_r = 10 kHz) of the 50% *w/w* dispersion of ebselen in PVP-VA. (**b**) ^{77}Se CP-MAS spectra (ν_r = 14 kHz) comparing the centerband of the 50% *w/w* dispersion of ebselen in PVP-VA with that of crystalline ebselen. Spectra were obtained at 9.4 T and 273 K.

dimethylselenide performed using a locally-dense 6-311++G (3df) basis set for the Se atom and 6-311++G(2d,p) basis sets on the other atoms. From this, calculated CST principal values of δ_{11}=1725 ppm, δ_{22}=710 ppm, and δ_{33}=156 ppm are obtained. The calculated and experimental principal components of the CST are generally in good agreement, with only the δ_{33} value subject to a significant deviation, suggesting that the experimentally-measured values reported here are to be expected for selenium in the chemical environment seen in ebselen. The inclusion of the second ebselen molecule in the cluster was found to greatly improve the agreement between calculated and experimental CSTs. Although not the focus of the present work, the use of more accurate basis sets and more sophisticated relativistic effects methods would likely improve the calculated ^{77}Se CST results (43,44).

^{1}H SSNMR and 2D SSNMR Experiments

In Fig. 7, the ^{1}H SSNMR spectrum at 700 MHz of the 50% *w/w* ebselen dispersion in PVP-VA is shown in comparison to crystalline ebselen and PVP-VA. At this field, three distinct resonances are resolved in the dispersion and are assigned to the aromatic protons in ebselen, the protons at positions f and h in PVP-VA, and the remaining aliphatic protons in PVP-VA. The use of windowed DUMBO ^{1}H homonuclear decoupling was attempted at the same field (not shown) (34). However, this did not offer any improvement in ^{1}H resolution, most likely because the ^{1}H spectrum is dominated by ABMS, which is also responsible for the relatively broad resonances observed in the ^{13}C spectra discussed in the previous section. The resonances can be assigned as shown in Fig. 7 to the aromatic protons as a group and to protons in PVP-VA with distinct chemical shifts. The resolution of these ^{1}H spectra is sufficient to distinguish the two individual components of the nanocrystalline dispersion, which is helpful for the 2D analysis that follows. An unknown peak is observed at about 0.2 ppm in the ^{1}H DP-MAS spectrum of crystalline ebselen. This peak was also observed in $CDCl_3$ solution at 0.081 ppm, and is likely due to contamination of the commercial sample with a minor process impurity or with silicone grease (60). This impurity was not detected in the dispersion and may have evaporated or sublimed during drying.

^{1}H 2D spin diffusion experiments were performed at a variety of mixing times to detect interactions between the ^{1}H resonances assigned to ebselen and PVP-VA. The combination of strong magnetic dipolar couplings between ^{1}H nuclei and the large molar ratio of hydrogen in organic solids typically leads to efficient ^{1}H spin diffusion processes in these materials (14). A 2D method in which magnetization is stored longitudinally during the mixing period is an efficient method for detecting spin diffusion between components that are resolved by fast MAS, as in the present case, or by homonuclear decoupling, which may have advantages in cases where ABMS is less significant. A ^{1}H 2D spin diffusion experiment using fast MAS was recently applied to a similar situation to detect spin diffusion between the components in spray-dried nanoparticles (61). In Fig. 8, the results of ^{1}H 2D spin diffusion experiments performed on the 50% dispersion of ebselen in PVP-VA are shown. The ^{1}H 2D spin diffusion sequence used here is also commonly referred to in the literature as a NOESY experiment (for nuclear Overhauser effect spectroscopy), as it utilizes essentially the same pulse sequence, although the present usage does not involve any application of the nuclear Overhauser effect (61). Each ^{1}H 2D spin diffusion experiment shown in Fig. 8 required 1.5 h to execute. As the spin diffusion time (t_{SD}) is increased from 100 μs to 50 ms, aromatic-aliphatic correlations are observed between the nanocrystalline ebselen and the surrounding PVP-VA. The spin diffusion is observed to be essentially complete when t_{SD} reaches 50 ms. This result provides direct confirmation that the nanocrystalline ebselen phase is in intimate contact with the PVP-VA in the dispersion, and is consistent with the 35–60 nm domain size range assessed by PXRD.

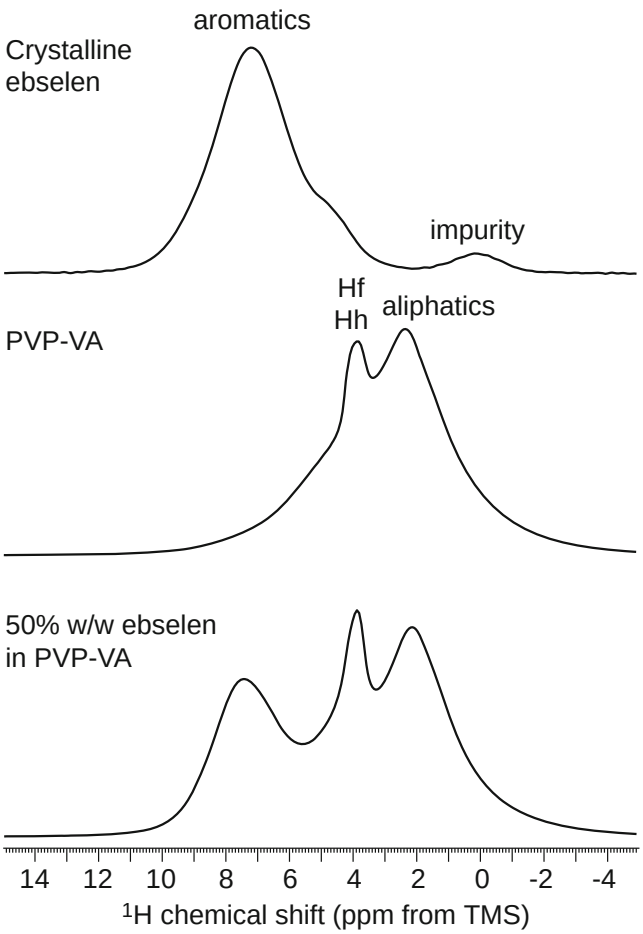

Fig. 7 ^{1}H DP-MAS spectra (ν_r=35 kHz) of ebselen, ebselen PVP-VA, and PVP-VA. Spectra were obtained at 16.4 T and 273 K.

The dispersion of ebselen in PVP-VA presents a favorable sample for high-field ^{1}H NMR analysis because of the resolution available in the ^{1}H MAS spectrum, which fundamentally arises from the presence of only aromatic proton environments in ebselen and aliphatic proton environments in PVP-VA. Other pharmaceutical materials of greater complexity may also still be accessible using fast MAS or by additional use of ^{1}H homonuclear decoupling methods (34). However, the presence of a wide variety of aromatic and aliphatic functional groups in most APIs is likely to present a challenge in achieving adequate ^{1}H resolution for some materials. In these cases, the additional resolution available from ^{13}C observation can be harnessed to detect long-range spin diffusion. One approach is to detect ^{1}H-^{1}H spin diffusion via ^{1}H-^{13}C dipolar correlation in a 2D HETCOR experiment. The conventional CP-HETCOR pulse sequence (35) used for characterization of interactions on the 10 Å scale in amorphous molecular dispersions (8,9) can be modified to account for the longer distances involved in dealing with nanocrystalline domains. This modification is needed because the times needed for spin diffusion to occur in nanoscale materials can range into the tens of ms or beyond, as seen earlier with the spectra in Fig. 8. Spin diffusion occurs in the conventional CP-HETCOR pulse sequence while the ^{1}H nuclei are spin locked under high RF power conditions, and long duration spin locks of >50 ms are beyond the capabilities of SSNMR instrumentation and also are likely to exceed the ^{1}H T_1 relaxation time in the rotating frame ($T_{1\rho}$). For nanocrystalline systems, ^{1}H spin diffusion can instead be allowed to occur by adding a special period wherein the ^{1}H magnetization is stored along the z-axis. This avoids

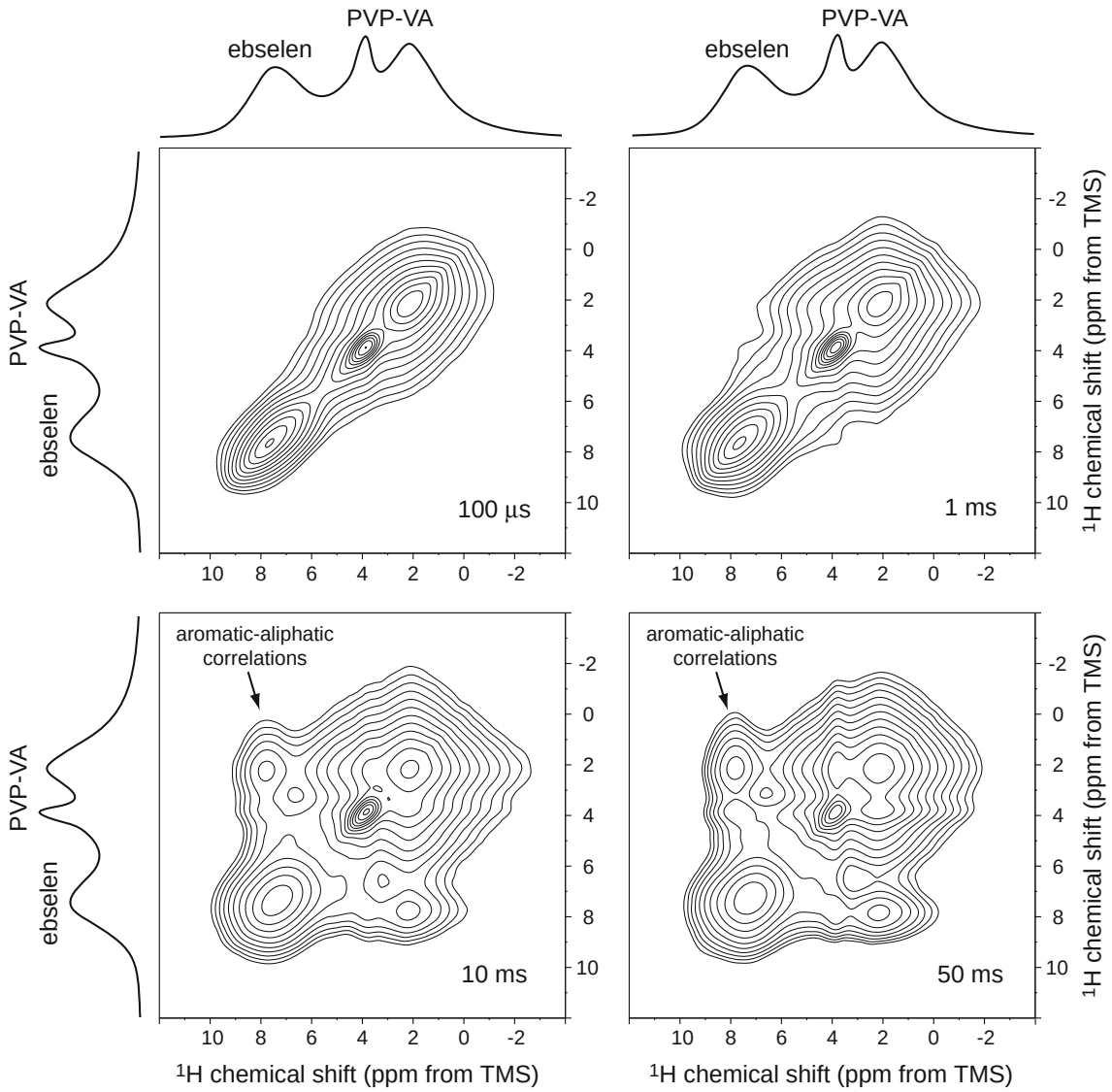

Fig. 8 2D ^{1}H spin diffusion spectra (ν_r=35 kHz) of the 50% *w/w* dispersion of ebselen in PVP-VA. The spectra were obtained using different spin diffusion mixing periods (t_{SD}) of 100 μs, 1 ms, 10 ms, and 50 ms. The ^{1}H DP-MAS spectrum obtained at the same spinning rate and shown in Fig. 7 is plotted along the F_1 (vertical) and F_2 (horizontal) axes. Spectra were obtained at 16.4 T and 273 K.

the use of RF power during spin diffusion and also takes advantage of the preservation of signal because of longer ^{1}H T_1 relaxation times instead of generally much shorter ^{1}H $T_{1\rho}$ times. A modified ^{1}H-^{13}C CP-HETCOR pulse sequence suitable for the study of nanocrystalline systems is depicted in Fig. 9. The approach used here adds a spin diffusion period before a 200 μs contact time. Because of the short contact time only limited spin diffusion occurs during this period. It is possible to eliminate spin diffusion during the contact time entirely using Lee-Goldburg CP (LGCP) transfers matched to the -1 Hartman-Hahn sideband (62), as was demonstrated previously in studies of amorphous dispersions (8). However, this reduces sensitivity and is unnecessary here. A similar modification to another HETCOR pulse sequence was recently applied to study spin diffusion in liquid crystalline systems (63).

The results of the modified ^{1}H-^{13}C CP-HETCOR experiment on the dispersion of interest here are shown in Fig. 10. With t_{SD} set to 1 ms, spin diffusion is observed between aromatic carbon positions in ebselen and aliphatic proton positions in PVP-VA. Spin diffusion is initially observed to involve carbons in the 130 ppm region, which is consistent with the earlier observation of enhanced signal intensity to C6 seen in Fig. 5, where a 2 ms contact time was used during which short-range spin diffusion can occur. These combined results suggest that the aromatic rings of ebselen are in particularly close contact with PVP-VA at the nanocrystalline interface, possibly interacting through van der Waals (dispersive) forces. This effect could also be enhanced by a small amount of ebselen dissolved in PVP-VA as a molecular dispsersion, as suggested by Raman spectral mapping. With t_{SD} increased to 10 ms, the reverse interactions between carbon positions in PVP-VA and aromatic proton positions in ebselen are observed as shown in Fig. 10. The spin diffusion is essentially complete when t_{SD} reaches 50 ms by comparison with a spectrum obtained at 100 ms (not shown). After this point, the overall signal begins to decay because of ^{1}H T_1 relaxation. Because of the reduced sensitivity and natural abundance of the ^{13}C isotope, each 2D spin diffusion experiment shown in Fig. 10 required 12 h to execute, considerably longer than the much more sensitive ^{1}H experiments used to collect the data in Fig. 8.

The observation that spin diffusion is complete at t_{SD}= 50 ms can be shown to be consistent with the presence of nanometer-scale domains by considering an order-of-magnitude estimate of the domain size effect on the build-up of ^{1}H spin diffusion (64–66). Expressions have been derived for spin diffusion from a point in three dimensions under the assumption of spherical particles for systems not exhibiting significant molecular dynamics (64). A spin diffusion length (L_{SD}) can be estimated for a particular experimental t_{SD} using the following equation (64–66):

$$\langle L_{SD} \rangle = 6\ D\ t_{SD}$$

The spin diffusion coefficient (D) in this equation may be estimated as $D = \langle l_0^2 \rangle / T_2$, where l_0 is the distance between protons (typically about 0.1 nm) and T_2 is the spin-spin relaxation time. Under static (non-spinning) conditions, a T_2 value of 31 μs was calculated from the linewidth of the ^{1}H spectrum obtained at 700.13 MHz for the 50% dispersion of ebselen in PVP-VA. Using this T_2 value and a t_{SD} of 50 ms, a value of approximately 10 nm is obtained for L_{SD}. This order-of-magnitude estimate is consistent with the PXRD results in the previous section, but is subject to the aforementioned approximations as well as the known reduction in D caused by the use of MAS during t_{SD} (67). For example, with spinning at v_r=12.5 kHz, the T_2 value is increased to approximately 130 μs and the estimated L_{SD} is reduced to approximately 5 nm at the same t_{SD}. Although not pursued here, it is possible to calibrate spin diffusion data against results obtained via other techniques to allow for more accurate estimation of domain sizes (14).

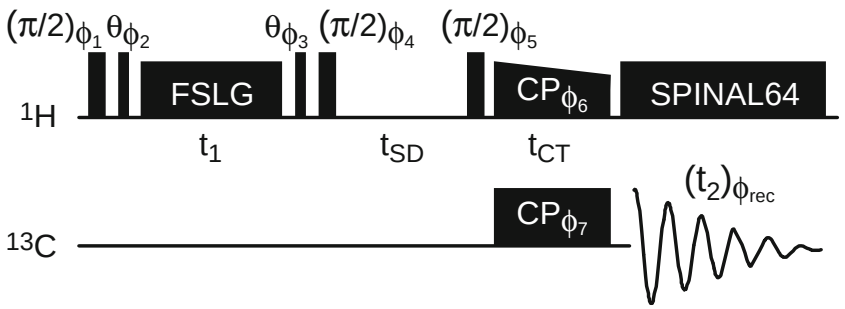

Fig. 9 Modified SSNMR pulse sequence used to obtain ^{1}H-^{13}C CP-HETCOR spectra with a separate spin diffusion period for nm-scale applications. Dark blocks represent radiofrequency pulses. CP refers to a cross-polarization transfer period with a ramp on the ^{1}H channel and a contact time (t_{CT}) of 200 μs as described in the text. FSLG and SPINAL64 refer to homonuclear and heteronuclear decoupling sequences and t_{SD} refers to the spin diffusion period (see text). Time periods t_1 and t_2 refer to the time-domain periods used to produce the 2D correlation spectrum. The pulse duration θ aligns the magnetization at the magic angle (35). The phase cycle is as follows (with 0 corresponding to a 0° phase shift, 1 corresponding to a 90° phase shift, 2 corresponding to a 180° phase shift, and 3 corresponding to a 270° phase shift): ϕ_1=(1 3), ϕ_2=(1), ϕ_3=(3), ϕ_4=(3 1 0 2 1 3 2 0), ϕ_5=(1 3 2 0 3 1 0 2), ϕ_6=(0), ϕ_7=(0 0 2 2 1 1 3 3), and ϕ_{rec}=(0 2 2 0 1 3 3 1).

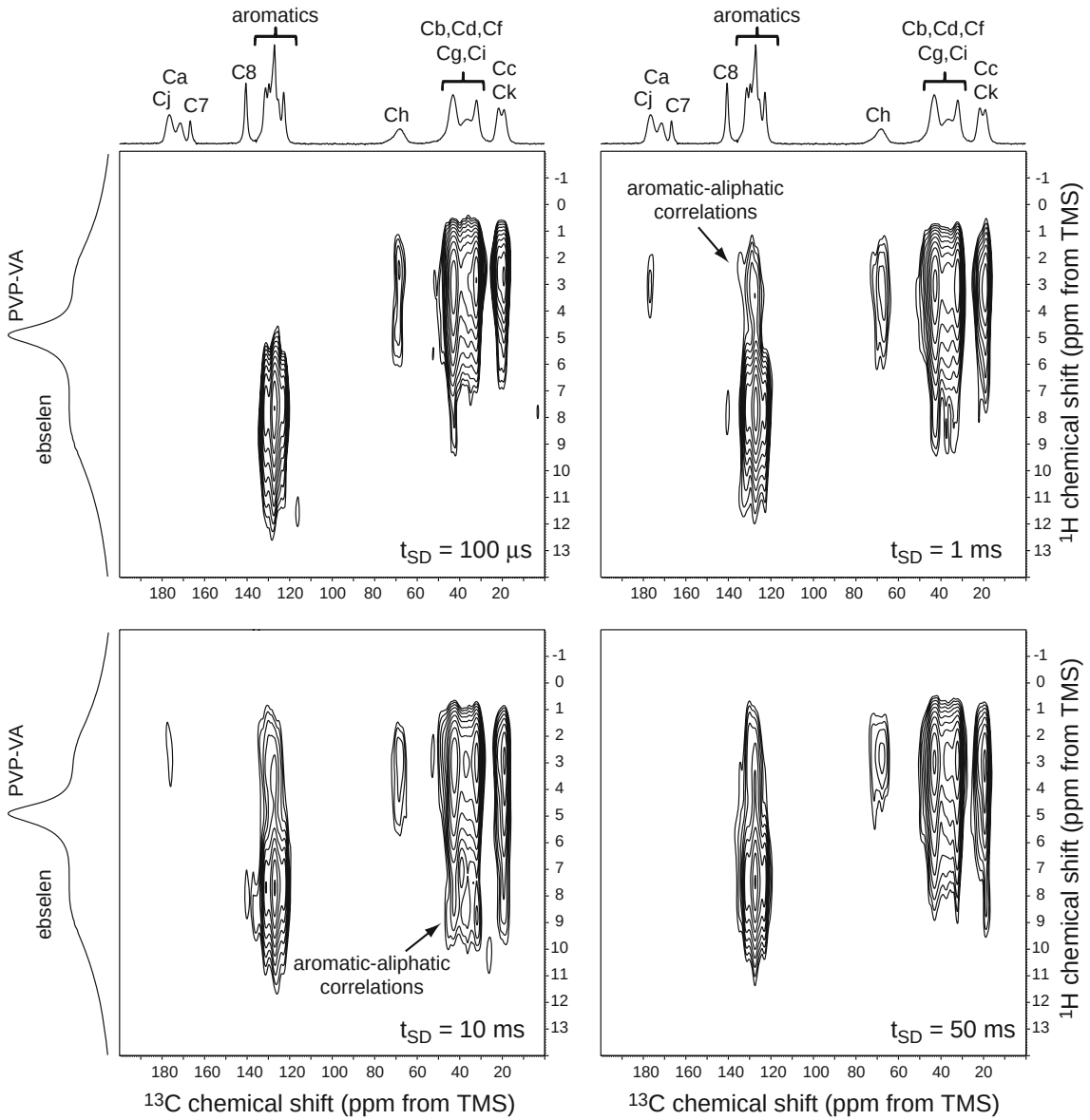

Fig. 10 2D ^{1}H-^{13}C CP-HETCOR spectra (ν_r = 12.5 kHz) obtained using different spin diffusion mixing periods (t_{SD}) of 100 μs, 1 ms, 10 ms, and 50 ms. After the spin diffusion mixing period, a 200 μs contact time (t_{CT}) was used. A ^{1}H DP-MAS spectrum (ν_r = 14 kHz) is plotted along the F_1 (vertical) axis, and a ^{13}C CP-TOSS spectrum (ν_r=8 kHz) is shown along the F_2 (horizontal) axis. The ^{1}H DP-MAS spectrum shows reduced resolution in comparison to the spectrum in Fig. 7 because of the lower field and reduced spinning rate. All spectra were obtained at 9.4 T and 273 K.

^{1}H T_1 analysis is widely used to show the presence of different domains in pharmaceutical applications of SSNMR because ^{1}H spin diffusion leads to a single T_1 value (68). When nanometer-sized domains are present, this is not expected to be the case (64–66). This result was confirmed during the course of this work using ^{1}H T_1 saturation recovery experiments. With ν_r set to 15 kHz, the slowest speed at which reasonable resolution in the ^{1}H spectrum could be obtained, the aromatic ebselen signal exhibited a ^{1}H T_1 of 5.2 s while the aliphatic PVP-VA signal exhibited a ^{1}H T_1 of 3.4 s. After ν_r was increased to 35 kHz, these values were largely unchanged at 5.5 s and 3.3 s, respectively. For comparison, the ^{1}H T_1 value of input crystalline ebselen was 12 s with ν_r=8 kHz. Although this behavior can also be used to estimate domain sizes when the nanometer-sized domains have statistically different T_1 values (8,64–66), the possibility of coincidental T_1 values suggests that the 2D spin diffusion experiments described above will be more useful in practice for studying nanocrystalline domains in drug-polymer dispersions.

CONCLUSIONS

A novel nanocrystalline dispersion of ebselen in PVP-VA was characterized by a range of complementary analytical methods. The nanocrystalline domains of ebselen were

determined to be on the order of 35 to 60 nm by PXRD. Confocal Raman microscopic mapping was used to assess the overall homogeneity of the dispersion, and also to detect a small fraction of ebselen that may be dissolved in PVP-VA. This fraction, which was not detectable by other techniques, was observed by detection of a band that did not correspond to either crystalline ebselen or PVP-VA, and correlation of the area of this band with the distribution of the two components. ^{1}H, ^{13}C, and ^{77}Se 1D SSNMR techniques were also used to characterize the dispersion, confirming that the ebselen was predominantly present in the crystalline state. The experimental ^{77}Se CST parameters for ebselen were determined and a theoretical verification was reported.

2D SSNMR techniques were used to show close association between PVP-VA and ebselen. These techniques detected some evidence of preferential association between PVP-VA and specific aromatic positions in the ebselen molecule via enhanced CP and spin diffusion. The utility of the 2D SSNMR techniques demonstrated here should extend to other nanocrystalline drug-polymer dispersions, allowing for detection of longer-range spin diffusion and interactions between drug and polymer. The 2D SSNMR approach demonstrated here extends previous work on amorphous dispersions with molecular- and nanometer-scale mixing between components (8,9). High-field ^{1}H SSNMR analysis of spin diffusion was found to be a useful tool for analysis of the crystalline dispersion of ebselen and PVP-VA. Lower static field strengths can also be used for spin diffusion analysis, particularly if homonuclear ^{1}H decoupling and ^{13}C-detection are applied to increase resolution, albeit at the expense of sensitivity. Homonuclear ^{1}H decoupling was ineffective for the crystalline phase of ebselen examined in this work because of strong ABMS effects, but is likely to be effective for other APIs with a mixture of aliphatic and aromatic functional groups. Finally, it is notable that all analytical work shown here was accomplished using less than 80 mg of the dispersion of interest, which allows for use of these approaches even when API supply is limited, such as during early pre-clinical drug development.

REFERENCES

1. Janssens S, Van den Mooter G. Physical chemistry of solid dispersions. J Pharm Pharmacol. 2009;61:1571–86.
2. Friesen DT, Shanker R, Crew M, Smithey DT, Curatolo WJ, Nightingale JAS. Hydroxypropyl methylcellulose acetate succinate-based spray-dried dispersions: an overview. Mol Pharm. 2008;5:1003–19.
3. Buttini F, Colombo P, Wenger MPE, Mesquida P, Marriott C, Jones SA. Back to basics: the development of a simple, homogenous, two-component dry-powder inhaler formulation for the delivery of budesonide using miscible vinyl polymers. J Pharm Sci. 2008;97:1257–67.
4. Traynor MJ, Zhao Y, Brown MB, Jones SA. Vinyl polymer-coated lorazepam particles for drug delivery to the airways. Int J Pharm. 2011;410:9–16.
5. Qian F, Tao J, Desikan S, Hussain M, Smith RL. Mechanistic investigation of Pluronic-based nano-crystalline drug-polymer solid dispersions. Pharm Res. 2007;24:1551–60.
6. Raghavan SL, Trividic A, Davis AF, Hadgraft J. Crystallization of hydrocortisone acetate: influence of polymers. Int J Pharm. 2001; 212:213–21.
7. Laaksonen T, Liu P, Rahikkala A, Peltonen L, Kauppinen EI, Hirvonen J, *et al.* Intact nanoparticulate indomethacin in fast-dissolving carrier particles by combined wet milling and aerosol flow reactor methods. Pharm Res. 2011;28:2403–11.
8. Pham TN, Watson SA, Edwards AJ, Chavda M, Clawson JS, Strohmeier M, *et al.* Analysis of amorphous solid dispersions using 2D solid-state NMR and ^{1}H T_1 relaxation measurements. Mol Pharm. 2010;7:1667–91.
9. Patel JR, Carlton RA, Yuniatine F, Needham TE, Wu L, Vogt FG. Preparation and structural characterization of amorphous spray-dried dispersions of tenoxicam with enhanced dissolution. J Pharm Sci. 2011;101:641–63.
10. Qian F, Huang J, Zhu Q, Haddadin R, Gawel J, Garmise R, *et al.* Is a distinctive single T_g a reliable indicator for the homogeneity of amorphous solid dispersion? Int J Pharm. 2010;395:232–5.
11. Ernst RR, Bodenhausen G, Wokaun A. Principles of nuclear magnetic resonance in one and two dimensions. New York: Oxford University Press; 1987. p. 535–8.
12. Caravatti P, Deli JA, Bodenhausen G, Ernst RR. Direct evidence of microscopic homogeneity in disordered solids. J Am Chem Soc. 1982;104:5506–7.
13. Meier BH. Polarization transfer and spin diffusion in solid-state NMR. Adv Magn Opt Reson. 1994;18:1–116.
14. Cheung TTP. Spin diffusion in solids. In: Harris RK, Grant DM, editors. The encyclopedia of NMR. New York: Wiley; 1996. p. 4518–24.
15. Schmidt-Rohr K, Spiess HW. Multidimensional solid-state NMR and polymers. London: Academic; 1994.
16. Brown S. Applications of high-resolution ^{1}H solid-state NMR. Solid State Nucl Magn Reson. 2012;41:1–27.
17. Harris RK, Hodgkinson P, Zorin V, Dumez JN, Elena-Herrmann B, Emsley L, *et al.* Computation and NMR crystallography of terbutaline sulfate. Magn Reson Chem. 2010;48:S103–12.
18. Pickard CJ, Salager E, Pintacuda G, Elena B, Emsley L. Resolving structures from powders by NMR crystallography using combined proton spin diffusion and plane wave DFT calculations. J Am Chem Soc. 2007;129:8932–3.
19. Sakellariou D, Lesage A, Emsley L. Proton-Proton Constraints in Powdered Solids from ^{1}H-^{1}H-^{1}H and ^{1}H-^{1}H-^{13}C Three-Dimensional NMR Chemical Shift Correlation Spectroscopy. J Am Chem Soc. 2001;123:5604–5.
20. Hu WG, Schmidt-Rohr K. Characterization of ultradrawn polyethylene fibers by NMR: crystallinity, domain sizes and a highly mobile second amorphous phase. Polymer. 2000;41:2979–87.
21. Raitza M, Wegmann J, Bachmann S, Albert K. Investigating the surface morphology of triacontyl phases with spin-diffusion solid-state NMR spectroscopy. Angew Chem Int Ed. 2000;39:3486–9.
22. Parnham M, Sies H. Ebselen: prospective therapy for cerebral ischaemia. Exp Opin Invest Drugs. 2000;9:607–19.
23. Nagase Y, Suzuki N, Yamauchi H, Kim S, Wada K, Arima H, *et al.* Inclusion complexation of a seleno-organic antioxidant, ebselen, with cyclodextrins in aqueous solution. J Incl Phenom Macro Chem. 2002;44:107–10.
24. Breitenback J, Schrof W, Neumann J. Confocal Raman spectroscopy: analytical approach to solid dispersions and mapping of drugs. Pharm Res. 1999;16:1109–13.

25. Pawley GS. Unit-cell refinement from powder diffraction scans. J Appl Cryst. 1981;14:357–61.
26. Dupont PL, Dideberg O, Jacquemin P. Structures de l'ebselen (phenyl-2 2H-benzisoselenazole-l,2 one-3) (I) et de l'acetonyl-se1eno-2 benzanilide (II). Acta Cryst. 1990;C46:484–6.
27. Le Bail A. Whole powder pattern decomposition methods and applications - A retrospection. Powder Diffract. 2005;20:316–26.
28. Metz G, Wu X, Smith SO. Ramped-amplitude cross-polarization in magic-angle spinning NMR. J Magn Reson A. 1994;110:219–27.
29. Antzutkin ON. Sideband manipulation in magic-angle spinning NMR. Prog NMR Spectros. 1999;35:203–66.
30. Fung BM, Khitrin AK, Ermolaev K. An improved broadband decoupling sequence for liquid crystals and powders. J Magn Reson. 2000;142:97–101.
31. Opella SJ, Frey MH. Selection of non-protonated carbon resonances in solid-state NMR. J Am Chem Soc. 1979;101:5854–6.
32. Earl WL, Vanderhart DL. Measurement of ^{13} chemical shifts in solids. J Magn Reson. 1982;48:35–54.
33. Demko BA, Wasylishen RE. Solid-state selenium-77 NMR. Prog NMR Spectros. 2009;54:208–38.
34. Lesage A, Sakellariou D, Hediger S, Elena B, Charmont P, Steuernagel S, *et al.* Experimental aspects of proton NMR spectroscopy in solids using phase-modulated homonuclear dipolar decoupling. J Magn Reson. 2003;163:105–13.
35. van Rossum BJ, Förster H, de Groot HJM. High-field and high-speed CP-MAS ^{13}C NMR heteronuclear dipolar-correlation spectroscopy of solids with frequency-switched Lee-Goldburg homonuclear decoupling. J Magn Reson. 1997;124:516–9.
36. Delley B. An all-electron numerical method for solving the local density functional for polyatomic molecules. J Chem Phys. 1990;92:508–17.
37. Delley B. From molecules to solids with the DMol3 approach. J Chem Phys. 2000;113:7756–64.
38. Boese AD, Handy NC. A new parametrization of exchange-correlation generalized gradient approximation functionals. J Chem Phys. 2001;114:5497–503.
39. Flurchick KM. DFT functionals and molecular geometries. Chem Phys Lett. 2006;421:540–3.
40. Gaussian 09, Revision B.01, Frisch MJ, Trucks GW, Schlegel HB, Scuseria GE, Robb MA, *et al.* Gaussian, Inc., Wallingford CT. 2010.
41. Becke AD. Density-functional thermochemistry. III. The role of exact exchange. J Chem Phys. 1993;98:5648–52.
42. Koch W, Holthausen MC. A chemist's guide to density functional theory. Weinheim: Wiley-VCH; 2001.
43. Nakanishi W, Hayashi S, Katsura Y, Hada M. Relativistic effect on ^{77}Se NMR chemical shifts of various selenium species in the framework of zeroth-order regular approximation. J Phys Chem A. 2011;115:8721–30.
44. Jameson CJ, de Dios AC. Theoretical and physical aspects of nuclear shielding. Nuc Magn Reson. 2007;36:50–71.
45. McCusker LB, von Dreele RB, Cox DE, Louër D, Scardi P. Rietveld refinement guidelines. J Appl Cryst. 1999;32:36–50.
46. Allen FH, Motherwell WDS. Applications of the Cambridge Structural Database in organic chemistry and crystal chemistry. Acta Cryst. 2002;B58:407–22.
47. Langford JI, Wilson AJC. Scherrer after sixty years: a survey and some new results in the determination of crystallite size. J Appl Cryst. 1978;11:102–13.
48. Bergese P, Colombo I, Gervasoni D, Depero LE. Melting of nanostructured drugs embedded into a polymeric matrix. J Phys Chem B. 2004;108:15488–93.
49. Liu X, Yang P, Jiang Q. Size effect on melting temperature of nanostructured drugs. Mater Chem Phys. 2007;103:1–4.
50. Gouadec G, Columban P. Raman spectroscopy of nanomaterials: how spectra relate to disorder, particle size and mechanical properties. Prog Cryst Growth Charact Mater. 2007;53:1–56.
51. Kalinowski HO, Berger S, Braun S. Carbon-13 NMR spectroscopy. New York: Wiley; 1987.
52. VanderHart DL. Magnetic susceptibility and high resolution NMR of liquids and solids. In: Harris RK, Grant DM, editors. The encyclopedia of NMR. New York: Wiley; 1996. p. 2938–46.
53. Robbins AJ, Ng WTK, Jochym D, Keal TW, Clark SJ, Tozer DJ, *et al.* Combining insights from solid-state NMR and first principles calculation: applications to the ^{19}F NMR of octafluoronaphthalene. Phys Chem Chem Phys. 2007;9:2389–96.
54. Barich DH, Davis JM, Schieber LJ, Zell MT, Munson EJ. Investigation of solid-state NMR line widths of ibuprofen in drug formulations. J Pharm Sci. 2006;95:1586–94.
55. Wiles JA, Phadke AS, Bradbury BJ, Pucci MJ, Thanassi JA, Deshpande M. Selenophene-containing inhibitors of Type IIA bacterial topoisomerases. J Med Chem. 2011;54:3418–25.
56. Potrzebowski MJ, Katarzynski R, Ciesielski W. Selenium-77 and carbon-13 high-resolution solid-state studies NMR of selenomethionine. Mag Reson Chem. 1999;37:173–81.
57. Sarma BK, Mugesh G. Antioxidant activity of the anti-inflammatory compound ebselen: A reversible cyclization pathway via selenenic and seleninic acid intermediates. Chem Eur J. 2008;14:10603–14.
58. Orendt AM, Facelli JC. Solid state effects on NMR chemical shifts. Ann Rep NMR Spectros. 2007;62:115–78.
59. Harris RK, Hodgkinson P, Pickard CJ, Yates JR, Zorin V. Chemical shift computations on a crystallographic basis: some reflections and comments. Magn Reson Chem. 2007;45:S174–86.
60. Gottlieb HE, Kotlyar V, Nudelman A. NMR chemical shifts of common laboratory solvents as trace impurities. J Org Chem. 1997;62:7512–5.
61. Io T, Fukami T, Yamamoto K, Suzuki T, Xu J, Tomono K, *et al.* Homogeneous nanoparticles to enhance the efficiency of a hydrophobic drug, antihyperlipidemic probucol, characterized by solid-state NMR. Mol Pharm. 2010;7:299–305.
62. van Rossum BJ, de Groot CP, Ladizhansky V, Vega S, de Groot HJM. A method for measuring heteronuclear (^{1}H-^{13}C) distances in high speed MAS NMR. J Am Chem Soc. 2000;122:3465–72.
63. Xu J, Smith PES, Soong R, Ramamoorthy A. A proton spin diffusion based solid-state NMR approach for structural studies on aligned samples. J Phys Chem B. 2011;115:4863–71.
64. Henrichs PM, Tribone J, Massa DJ, Hewitt JM. Blend miscibility of bisphenol A polycarbonate and poly(ethylene terephthalate) as studied by solid-state high-resolution ^{13}C NMR spectroscopy. Macromolecules. 1988;21:1282–91.
65. Schantz S, Ljungqvist N. Structure and dynamics in polymer blends: a ^{13}C CPMAS NMR study of poly(3-octylthiophene)/poly(phenylene oxide). Macromolecules. 1993;26:6517–24.
66. McBrierty VJ, Douglass DC. Recent advances in the NMR of solid polymers. J Polym Sci Macromol Rev. 1981;16:295–366.
67. Krushelnitsky A, Brauniger T, Reichert D. ^{15}N spin diffusion rate in solid-state NMR of totally enriched proteins: the magic angle spinning frequency effect. J Magn Reson. 2006;182:339–42.
68. Zumbulyadis N, Antalek B, Windig W, Scaringe RP, Lanzafame AM, Blanton T, *et al.* Elucidation of polymorph mixtures using solid-state ^{13}C CP/MAS NMR spectroscopy and direct exponential curve resolution algorithm. J Am Chem Soc. 1999;121:11554–7.